



<http://www.diva-portal.org>

## Postprint

This is the accepted version of a paper published in *Journal of Physical Chemistry B*. This paper has been peer-reviewed but does not include the final publisher proof-corrections or journal pagination.

Citation for the original published paper (version of record):

Kunnus, K., Zhang, W., Delcey, M G., Pinjari, R V., Miedema, P S. et al. (2016)  
Viewing the Valence Electronic Structure of Ferric and Ferrous Hexacyanide in Solution from the Fe and Cyanide Perspectives.  
*Journal of Physical Chemistry B*, 120(29): 7182-7194  
<http://dx.doi.org/10.1021/acs.jpcc.6b04751>

Access to the published version may require subscription.

N.B. When citing this work, cite the original published paper.

Permanent link to this version:

<http://urn.kb.se/resolve?urn=urn:nbn:se:uu:diva-304444>

# Viewing the valence electronic structure of ferric and ferrous hexacyanide in solution from the Fe and cyanide perspectives

Kristjan Kunnus,<sup>1,2\*</sup> Wenkai Zhang,<sup>3‡</sup> Mickaël G. Delcey,<sup>4</sup> Rahul V. Pinjari,<sup>4</sup> Piter S. Miedema,<sup>1</sup> Simon Schreck,<sup>1,2&</sup> Wilson Quevedo,<sup>1</sup> Henning Schröder,<sup>1,2</sup> Alexander Föhlisch,<sup>1,2</sup> Kelly J. Gaffney,<sup>3</sup> Marcus Lundberg,<sup>4\*</sup> Michael Odelius,<sup>5\*</sup> Philippe Wernet,<sup>1\*</sup>

1 Institute for Methods and Instrumentation for Synchrotron Radiation Research, Helmholtz-Zentrum Berlin für Materialien und Energie GmbH, Albert-Einstein-Strasse 15, 12489 Berlin, Germany

2 Institut für Physik und Astronomie, Universität Potsdam, Karl-Liebknecht-Strasse 24/25, 14476 Potsdam, Germany

3 PULSE Institute, SLAC National Accelerator Laboratory, Menlo Park, CA 94025, USA

4 Department of Chemistry - Ångström laboratory, Uppsala University, 75120 Uppsala, Sweden

5 Department of Physics, Stockholm University, AlbaNova University Centre, 10691 Stockholm, Sweden

\*Correspondence to: [kkunnus@stanford.edu](mailto:kkunnus@stanford.edu), [wernet@helmholtz-berlin.de](mailto:wernet@helmholtz-berlin.de)

#Current address: PULSE Institute, SLAC National Accelerator Laboratory, Menlo Park, CA 94025, USA

‡ Current address: Department of Physics, Beijing Normal University, Beijing, 100875, China

& Current address: Department of Physics, Stockholm University, AlbaNova University Centre, 10691 Stockholm, Sweden

## Abstract:

The valence excited states of ferric and ferrous hexacyanide ions in aqueous solution were mapped with resonant inelastic X-ray scattering (RIXS) at the Fe  $L_{2,3}$ - and N K-edges. Probing of both the central Fe and the ligand N atoms enabled identification of the metal- and ligand-centered excited states, as well as ligand-to-metal and metal-to-ligand charge transfer excited states. *Ab initio* calculations utilizing the RASPT2 method was used to simulate the Fe  $L_{2,3}$ -edge RIXS spectra and enabled quantification of the covalency of both occupied and empty orbitals of  $\pi$  and  $\sigma$  symmetry. We find that  $\pi$  back-donation in the ferric complex is smaller compared to the ferrous complex. This is evidenced by the relative amount of Fe 3d character in the nominally  $2\pi$  CN $^-$  molecular orbital of 7% and 9% in ferric and ferrous hexacyanide, respectively. Utilizing the direct sensitivity of Fe  $L_{3}$ -edge RIXS to the Fe 3d character in the occupied molecular orbitals we also find that the donation interactions are dominated by  $\sigma$ -bonding. The latter is found to be stronger in the ferric complex with a Fe 3d contribution to the nominally  $5\sigma$  CN $^-$  molecular orbitals of 29% compared to 20% in the ferrous complex. These results are consistent with the notion that a higher charge at the central metal atom increases donation and decreases back-donation.

## Introduction

Transition metal coordination complexes are central constituents of many relevant homogeneous and biological catalysts and photoactive materials. In these systems the functionality is often governed by local changes of coordination, bonding, charge and spin state of the transition metal atom.<sup>1-6</sup> Particularly well suited for probing these local properties are X-ray spectroscopic methods due to their intrinsic sensitivity to the electronic structure in a local and element-specific manner.<sup>7</sup> Therefore, owing to the significant advance of related experimental technologies in recent years, X-ray spectroscopy techniques are becoming increasingly popular in the research of functional transition metal systems. Specially X-ray absorption spectroscopy (XAS) at the metal  $L_{2,3}$  and ligand K-edges of transition metal compounds is now well established.<sup>8,9</sup> In the present study we apply resonant inelastic X-ray scattering (RIXS) at the Fe  $L_{2,3}$  and the N K absorption edges to probe the valence orbital compositions of the occupied and unoccupied valence orbitals of iron hexacyanides in aqueous solution from both the metal and the ligand perspective. Utilizing quantum-chemical simulations of the Fe  $L_{2,3}$  RIXS spectra we disentangle the chemical, multiplet and core-hole effects. We carry out a comparative study of ferrous and ferric hexacyanide with the specific aim to understand the effect of the Fe charge state to the chemical bonding in these complexes.

Ferrous and ferric hexacyanides are prototypical back-bonding transition metal complexes. The ferrocyanide anion,  $[\text{Fe}(\text{CN})_6]^{4-}$ , contains  $\text{Fe}^{2+}$  with a nominally  $3d^6$  configuration, whereas the ferricyanide anion,  $[\text{Fe}(\text{CN})_6]^{3-}$ , contains  $\text{Fe}^{3+}$  with a nominally  $3d^5$  configuration. Both complexes can be well described as having an octahedral  $O_h$  molecular structure (with a small Jahn-Teller distortion in

ferricyanide).<sup>10,11</sup> The 3d orbitals are thus energetically split into  $t_{2g}$  and  $e_g$  orbitals by the strong-field  $\text{CN}^-$  ligands. Bonding between iron and the  $\text{CN}^-$  ligands has significant covalent character. It is dominated by the interaction of the partially occupied iron 3d orbitals with the occupied  $\text{CN}^-$  valence orbitals (electron donation) as well as with the unoccupied  $\text{CN}^-$  valence orbitals (back-donation).

Chemical bonding or, more generally, the valence electronic structure of iron hexacyanides has been studied in the past with various soft and hard X-ray methods. Solid-state samples were investigated using X-ray absorption spectroscopy (XAS) based on electron-yield detection at the Fe K-edge (Fe  $1s \rightarrow 4p$ ), at the Fe  $L_{2,3}$ -edge (Fe  $2p \rightarrow 3d$ ) and at the N K-edge (N  $1s \rightarrow 2p$ ).<sup>12-14</sup> Early solution-state Fe  $L_{2,3}$ -edge XAS studies were also reported<sup>15</sup> and more recently an Fe  $L_{2,3}$  and N K-edge RIXS study of ferrocyanide in solution combined with quantum-chemical calculations was published<sup>16</sup>. A detailed Fe  $L_{2,3}$ -edge XAS study was carried out by Hocking et al. where they used extensive semi-empirical charge-transfer multiplet (CTM) calculations to simulate spectral shapes with great accuracy.<sup>17</sup> Recently, several novel hard X-ray spectroscopy techniques have been applied for understanding back-bonding in iron hexacyanides complexes. Lundberg et al. (Ref. 18) utilized hard X-ray  $K\alpha$  RIXS at the quadrupole allowed  $1s \rightarrow 3d$  pre-resonance of the Fe K-edge to probe the covalency of solid state ferric and ferrous hexacyanide and successfully simulated the RIXS spectra of the  $2p^5 3d^{n+1}$  final states with the CTM model of Hocking et al. Recently, Penfold et al. applied the latter technique to probe the solvent effects in ferrous and ferric hexacyanide dissolved in water and ethylene glycol.<sup>19</sup> Non-resonant  $K\beta$  and valence-to-core X-ray emission spectroscopy (XES) studies were performed on solid samples of ferri- and ferrocyanide and combined with a density functional theory (DFT) based approach to disentangle the contributions of metal spin state, covalency and metal-ligand bond lengths.<sup>20,21</sup> The present knowledge of the valence electronic structure proved useful in picosecond time-resolved hard X-ray XAS<sup>22</sup> and XES<sup>23</sup> investigations of iron hexacyanides in solution and in the investigation of their redox properties in an electro-chemical cell at in operando conditions.<sup>24</sup>

The above mentioned hard X-ray XAS and XES spectroscopy techniques can be sensitive to chemical bonding. However the mechanism of sensitivity is relatively indirect, resulting from multiple-scattering resonances and dipole forbidden weak pre-resonance in Fe K-edge XAS<sup>7,25</sup> or from 2p-3d and 3p-3d Coulomb exchange interactions in core-to-core  $K\alpha$  and  $K\beta$  XES<sup>20,21,26</sup>. In both cases the considerable lifetime broadening of the 1s core hole further limits the information content. Specific details of bonding such as a delineation of donation and back-donation effects are not probed. Novel, but

experimentally more challenging hard X-ray techniques as mentioned above can be used to probe directly the valence orbitals: RIXS experiments at the Fe K-edge pre-resonance are sensitive to unoccupied Fe 3d character and valence-to-core XES probes directly occupied Fe 4p character of (nominally) non-bonding ligand valence orbitals.

In comparison to hard X-ray methods, soft X-ray spectroscopy techniques can provide complementary and more detailed information because the spectral features corresponding to dipole-allowed excitations to the valence orbitals are dominating with respect to the continuum excitations (e.g. in contrast to the Fe K-edge XAS) and the associated natural lifetime broadenings are significantly smaller. Fe  $L_{2,3}$ -edge XAS is dominated by dipole-allowed transitions from Fe 2p to unoccupied valence orbitals containing 3d character. XAS at the ligand K-edge probes the unoccupied 2p character of these orbitals. XES at these absorption edges probes the respective occupied valence orbitals. Soft X-ray RIXS thus offers the opportunity to efficiently probe the valence electronic structure by directly addressing both the occupied and unoccupied valence orbitals.

Despite these intrinsic advantages, soft X-ray XES and RIXS experiments on transition metal solutes are still relatively scarce due to experimental challenges. Only relatively recently in-vacuum methods for soft X-ray RIXS spectroscopy on liquids and solutions were developed<sup>27-31</sup> and typical count rates are low due to the small fluorescence yields and the considerable solvent absorption in the soft X-ray range. The latter is particularly important when dealing with dilute samples as typical for chemically/biologically relevant samples. The high solubility of iron hexacyanides in water make them appropriate model systems to test current experimental capabilities of solution phase soft X-ray RIXS. From a conceptual point of view they are ideally suited to test the concept of mapping out the valence electronic structure from both the metal and the ligand perspective by decomposing the valence orbitals into their constituents.

Engel et al. applied recently soft X-ray RIXS at the Fe  $L_{2,3}$ - and N K-edge to directly probe charge donation and back-donation in ferrocyanide aqueous solution.<sup>16</sup> Here we aim to refine, complement and extend these results both in terms of new experiments and new calculations by additionally addressing ferricyanide and by comparing both compounds in detail. Furthermore we recorded the full RIXS planes (in contrast to a limited number of XES or RIXS spectra at selected incident photon energies) both at the Fe  $L_{2,3}$  and the N K-edges. In addition, we improved the restricted active space self-consistent field (RASSCF) calculations for the Fe  $L_{2,3}$ -edge RIXS. The RASSCF method in combination with second-order perturbation theory (RASPT2) has become a powerful computational

tool for ab initio simulations of soft X-ray spectra of transition metal complexes.<sup>32,33</sup> A systematic RASPT2 study of L<sub>2,3</sub>-edge XAS spectra of Fe<sup>3+</sup> ions, including ferricyanide, was recently performed by Pinjari et al.<sup>34</sup> Here we extend these results to simulate the full Fe L<sub>2,3</sub>-edge RIXS planes of both ferri- and ferrocyanide. The same computational approach has been also applied for simulating the pre-edge features in the Fe K-edge XAS spectra.<sup>35</sup>

## **Methods**

### **Experimental details**

Measurements were carried out at the beamline U41-PGM at BESSYII of the Helmholtz-Zentrum Berlin (HZB). The experimental setup (FlexRIXS) with an in-vacuum liquid jet for sample delivery and a grazing incidence spherical grating Rowland spectrometer was described before.<sup>31</sup> Briefly, the spectrometer was operated in a slitless mode to increase the geometric acceptance, with the 20 μm jet diameter limiting the resolving power. The incident X-rays were linearly polarized and the emitted X-rays were detected in-plane of the incident polarization under 90° scattering angle.

K<sub>3</sub>[Fe(CN)<sub>6</sub>] and K<sub>4</sub>[Fe(CN)<sub>6</sub>]·3H<sub>2</sub>O salts were purchased from Sigma-Aldrich and used without further purification. The solutions with respective concentrations of 0.5 M and 0.33 M were prepared using deionized water. The sample in the probed volume of the jet is replaced continuously at a rate of approximately 1 MHz rate (1 ml/min flow rate, 20 μm liquid jet diameter, 20×40 μm<sup>2</sup> X-ray spot size). This eliminates the effect of beam damage to the sample during the measurements.<sup>15,24,36</sup>

RIXS maps were recorded while stepwise scanning the incident photon energy. At the Fe L-edge a photon energy range from 705 eV to 730 eV was scanned with a bandwidth of 0.5 eV for the incident radiation (step size 0.4 eV). The spectrometer resolution was 1 eV. Data accumulation times for ferric and ferrous solutions amounted to 6 h 20 min and 5 h 30 min, respectively. At the N K-edge, the scanned photon energy range was from 395 eV to 415 eV and the incident bandwidth was 0.22 eV (step size 0.1 eV). The spectrometer resolution was 0.5 eV. The data were collected within 3 h and 3 h 20 min for ferric and ferrous samples, respectively. At the Fe L-edge, the incident photon energy was calibrated with the XAS spectra in Hocking et al.<sup>17</sup> and at the N K-edge the calibration was done after XAS spectra in Vinogradov et al.<sup>14</sup> The photon energy scale for emitted X-rays was calibrated using the elastic scattering peaks.

## Computational details

Multi-configurational quantum chemical calculations for RIXS spectral simulations at the Fe  $L_{2,3}$ -edge were carried out in MOLCAS 8.0 software<sup>37</sup> in  $D_{2h}$  symmetry with inclusion of relativistic (scalar and spin-orbit coupling) effects as described in our previous XAS simulations<sup>34,38,39</sup> (using the ANO-RCC-VTZP basis set, notice the recently corrected basis set for carbon from Ref. 40). The  $[\text{Fe}(\text{CN})_6]^{3-/4-}$  complex geometries are re-optimized on the CASPT2(9/10,10) level<sup>41</sup> yielding the distances for the ferric (Fe-C=2×1.921 Å, 4×1.943 Å, Fe-N=2×3.107 Å, 4×3.127 Å) and for the ferrous (Fe-C=6×1.917 Å, Fe-N=6×3.113 Å) complexes.

For the spectrum simulations, RASSCF calculations<sup>42</sup> were performed with three Fe 2p orbitals in the first active space (RAS1, one hole allowed) and with ten valence orbitals in the second active space (RAS2). These included two  $5\sigma(e_g)$  orbitals, three  $t_{2g}$  orbitals, two  $e_g$  orbitals and three  $2\pi(t_{2g})$  orbitals which accommodate 9 (ferric) or 10 (ferrous) electrons (Figure 1). The RASSCF states were optimized within each  $D_{2h}$  symmetry class using a state-averaging procedure and a level shift of 1.0. Dynamical correlation effects were taken into account via second-order perturbation theory (PT2)<sup>43</sup> using an imaginary shift of 0.3. Spin-orbit interactions were calculated in the RASSI scheme<sup>44</sup>, including doublet and quartet states for ferricyanide and singlet and triplet states for ferrocyanide (sextet and quintet states were excluded as their effect to spectra was found to be insignificant). In total 1440 (800) valence-excited states and 2880 (1760) core-excited states were calculated for ferric (ferrous) hexacyanide. For comparison with experiment, core-excited state energies of ferricyanide and ferrocyanide were shifted by -3.3 eV and -3.1 eV, respectively. For ferricyanide, the presented spectra are an average of the calculated spectra of the two states corresponding to the ground state doublet in  $D_{2h}$  symmetry.

Charge-transfer multiplet (CTM)<sup>8,45,46</sup> RIXS calculations at the Fe  $L_3$ -edge were carried out using the parameters from the XAS calculations in Hocking et al. (Table S2 in the Supporting Information). Calculations were done in the  $C_{4h}$  point group symmetry to account for linear polarization of incident X-rays, but the latter effects were found negligible. The core-excited state energies were shifted to match with the first XAS resonance in the experiment.

For both the RASPT2 and the CTM calculations, RIXS spectra were simulated by multiplying absorption and emission dipole transition moments, i.e. interference effects were not included. The following broadening scheme for the calculated transitions was applied in order to facilitate comparison with experiment (values for the FWHM are

given): 0.5 eV Gaussian broadening taking into account the incident bandwidth, 0.3 eV (0.6 eV) Lorentzian natural lifetime broadening at the Fe L<sub>3</sub> (L<sub>2</sub>) edge, and 1.0 eV Gaussian broadening to account for the spectrometer resolution. An additional 0.5 eV Gaussian broadening for both X-ray absorption and RIXS spectra was introduced to account for inhomogeneous and vibrational broadening effects. Possible polarization effects of the incident radiation were checked for the RASPT2 calculations and found to be negligible.

## **Results**

In Figure 1 we show a qualitative valence molecular orbital (MO) diagram of iron hexacyanide complexes (a representative list of MOs from a SCF calculation is shown in the Supplementary Information, Table. S1). Electron donation between Fe<sup>2+/3+</sup> and the CN<sup>-</sup> ligands is carried by a covalent interaction of the Fe 3d MOs with 1π and 5σ ligand orbitals and back-donation is dominated by the 2π ligand orbitals (all three are mostly derived from 2p atomic orbitals of N and C). MOs derived from Fe 3d are depicted as t<sub>2g</sub> and e<sub>g</sub>, according to their respective symmetry class in the O<sub>h</sub> point group.

XAS and RIXS data of ferric and ferrous cyanide in aqueous solution measured over the whole Fe L<sub>2,3</sub>-edge are displayed in Figure 2. The XAS spectra were obtained by plotting the RIXS intensities integrated over all energy transfers versus incident photon energy. They thus correspond to partial-fluorescence yield (PFY) detected XAS (PFY-XAS). Discrepancies between our and previously published solution phase XAS spectra can be explained by possible beam damage in studies with solid or non-flown liquid samples<sup>15</sup> or by the established differences between x-ray absorption cross sections as measured in transmission and XAS spectra as measured by detecting fluorescence.<sup>47,48</sup> Saturation effects are negligible in the measured PFY-XAS spectra at the used solution concentrations. Spectral features in the RIXS maps can be categorized according to whether they correspond to valence excited final states resulting from filling of the core-hole created by photoabsorption or whether they correspond to ionized final states resulting from fluorescence decays preceded by Coster–Kronig decays (at the Fe L<sub>2</sub>-edge).<sup>33,49</sup> Being interested in probing the valence electronic structure and chemical bonding we concentrate in the following on analyzing the RIXS maps only at the Fe L<sub>3</sub>-edge because spectral features at the Fe L<sub>3</sub>-edge have higher intensity, smaller core-hole lifetime broadening and are not complicated by Coster-Kronig features.

In Figure 3 we compare in detail the RIXS maps and XAS spectra at the Fe L<sub>3</sub>- and N K-edges of ferric and ferrous hexacyanide. XAS spectra in Figure 3C-D reproduce well the features of the published electron yield XAS spectra measured from the solid

polycrystalline samples at the Fe  $L_{2,3}$ -edge<sup>17</sup> and N K-edge<sup>14</sup>. The ferricyanide complex has three prominent XAS resonances at the Fe  $L_3$ -edge which we denote  $a_M$  (705.6 eV),  $b_M$  (710.0 eV) and  $c_M$  (712.5 eV). The first resonance corresponds to excitations of an Fe 2p electron to the partially occupied  $t_{2g}$  manifold and the two resonances at higher energies can be tentatively assigned to excitations to  $e_g$  and  $2\pi(t_{2g})$  MOs. The assignments of all X-ray absorption resonances are summarized in Table 1.<sup>17</sup> The exact nature of the  $b_M$  and particularly the  $c_M$  resonances, however, is more complicated than the  $a_M$  resonance as is evident also from the comparably large width and the complex shapes of these resonances. It has been shown that mixing of  $[\text{Fe}2p(t_{1u})]^5[t_{2g}]^5[e_g]^0[2\pi(t_{2g})]^1$  with the doubly-excited  $[\text{Fe}2p(t_{1u})]^5[t_{2g}]^4[e_g]^2$  and  $[\text{Fe}2p(t_{1u})]^5[5\sigma(e_g)]^3[t_{2g}]^6[e_g]^1$  configurations contributes significantly.<sup>34</sup> Ferrocyanide with a filled  $[t_{2g}]^6$  manifold has two XAS resonances which analogously correspond to nominal excitations to  $e_g$  ( $b_M$ , 709.1 eV) and  $2\pi(t_{2g})$  ( $c_M$ , 711.2 eV) MOs (Table 1).<sup>17</sup> The high intensity of the  $c_M$  resonance has been attributed to intensity borrowing through mixing of  $[\text{Fe}2p(t_{1u})]^5[t_{2g}]^6[e_g]^0[2\pi(t_{2g})]^1$  with  $[\text{Fe}2p(t_{1u})]^5[t_{2g}]^5[e_g]^1[2\pi(t_{2g})]^1$  configurations.<sup>17</sup>

Our RASPT2 and CTM calculations for the Fe  $L_3$ -edge are displayed in Figure 4. Overall we find very good agreement of the calculated with the measured RIXS features for both ferri- and ferrocyanide. The calculated XAS spectra derived from the calculated RIXS maps as described for the experimental data are displayed in Figures 4E-F. For comparison the experimental spectra from Figure 3 are reproduced here (the calculated spectra are shifted to match with the lowest energy XAS resonance as described in the Methods section). For ferricyanide the relative energy, intensity and shape of the  $a_M$  and  $b_M$  resonances are reproduced nearly perfectly by the RASPT2 calculation. The  $c_M$  resonance is shifted by about 1 eV to higher energy and has higher intensity than in the experiment. However, the agreement is better compared to the CTM calculation reproduced from Hocking et al., which, in addition, does not describe as well the shapes of the  $b_M$  and  $c_M$  resonances. For ferrocyanide, both the RASPT2 and the CTM calculations reproduce very well the relative intensities of the  $b_M$  and  $c_M$  resonances, although the energy splitting is overestimated in the RASPT2 calculation by 0.75 eV and underestimated in the CTM calculation by 0.25 eV. Note that agreement of our RASPT2 calculation with experiment is improved compared to the calculation in Engel et al. where the intensity ratio of the  $b_M$  and  $c_M$  resonances is not well reproduced and the energy splitting is overestimated by about 2 eV.<sup>16</sup> This is primarily due to the limited flexibility in the active space and differences in orbital optimization. Additionally, in the present calculations we found that inclusion of the dynamical correlation reduces the

energy difference between the  $b_M$  and  $c_M$  resonances and increases the relative intensity of the  $c_M$  resonance.

In Figure 3C-D we show PFY-XAS spectra for the N K-edge as derived from the RIXS measurements. N K-edge XAS is sensitive to the N p character of the unoccupied MOs. It is evident that the dominant N K-edge XAS resonances at 399.5-399.6 eV correspond to transitions of N 1s electrons to the unoccupied CN $^-$   $2\pi$ -derived manifold of MOs (Figure 1 and Table 1). In addition to the anti-bonding  $2\pi(t_{2g})$  MO this manifold also includes non-bonding  $2\pi(t_{1u}, t_{2u}, t_{1g})$  MOs and in ferricyanide the  $c_L$  resonance at 399.6 eV and in ferrocyanide the  $c_L$  resonance at 399.5 eV can be assigned to transitions into these MOs.<sup>14,16</sup> In ferricyanide the weak  $a_L$  resonance at 396.1 eV (Figure 3C2) corresponds to excitation to the same partially filled  $t_{2g}$  MOs as the  $a_M$  resonance at the Fe  $L_3$ -edge. Evidently this resonance is not present in ferrocyanide. In addition, in ferricyanide we observe a clear shoulder at 398.5 eV on the low-energy side of the  $c_L$  main resonance which we label here with  $b_L$  (Figure 3C2). We propose that this  $b_L$  resonance corresponds to N 1s to  $e_g$  transitions (Table 1) resulting from intensity borrowing from  $2\pi$  MOs due to mixing between states of  $[N1s(e_g)]^3[t_{2g}]^5[e_g]^0[2\pi(t_{1u})]^1$  and  $[N1s(t_{1u})]^5[t_{2g}]^5[e_g]^1[2\pi(t_{1u})]^0$  configurations. We corroborate this assignment in the analysis of the RIXS features at the  $b_L$  shoulder below. The  $b_L$  feature is not visible in ferrocyanide (Figure 3D2), possibly because the respective states are closer to the dominant  $c_L$  resonance.

Direct comparison of Fe  $L_3$ -edge and N K-edge XAS spectra of ferricyanide (Fig. 3C1 and 3C2 and Table 1) reveals that the energy separation between the  $a_M$  and  $c_M$  resonances is much larger (6.9 eV) than between  $a_L$  and  $c_L$  (3.5 eV,) although the respective resonances correspond to excitations to nominally the same MOs. This can be explained by the different influence of Fe 2p and N 1s core-hole potentials to the different MOs. The Fe2p core-hole strongly interacts with the  $t_{2g}$  MOs with dominant Fe3d character thus increasing the energy difference between  $t_{2g}$  and  $2\pi$  MOs and explaining the large  $a_M$ - $c_M$  separation. In contrast, the N 1s core-hole interacts more strongly with the  $2\pi$  MOs, therefore leading to a decrease of the energy between  $t_{2g}$  and  $2\pi$  MOs and explaining the small  $a_L$ - $c_L$  separation.

The 4.4 eV energy separation of  $a_M$  and  $b_M$  resonances reflects the 10Dq of ferricyanide complex. It matches very well with the ground state 10Dq of 4.3 – 4.5 eV derived from UV/vis absorption experiments,<sup>50,51</sup> although contraction of metal 3d orbitals due to 2p core-hole leads typically to 10 – 20% reduction of the 10Dq.<sup>52</sup> Latter was also confirmed for ferri- and ferrocyanide by Hocking et al. who deduced 4.0 and 3.9 eV 10Dq values

from Fe  $L_{2,3}$ -edge XAS experiment, respectively.<sup>17</sup> The difference between  $a_M$ - $b_M$  separation and the core-excited  $10Dq$  value is explained by the multiplet effects, evident from the complex multiplet structure of the  $b_M$  resonance. Note however that metal  $L_{2,3}$ -edge RIXS probes the ground state  $10Dq$ , similarly to UV/vis absorption.<sup>33,53,54</sup>

The ferricyanide RIXS spectra taken at the  $a_M$  and  $a_L$  resonances (Figure 5A) show, in addition to the elastic scattering peak, a main RIXS peak denoted  $1a_{M,L}$  at an energy transfer of 4 eV with a weaker peak denoted  $2a_{M,L}$  at  $\sim 7$  eV. For excitation at the  $a_M$  resonance at 705.6 eV the elastic peak is intense due to six (nearly) degenerate  $t_{2g}$  electrons, thus allowing more resonant elastic scattering channels compared to excitation at the  $b_M$  and  $c_M$  resonances. The  $1a_{M,L}$  and  $2a_{M,L}$  peaks correspond to decays from dominantly ligand-centered MOs resulting in ligand-to-metal charge-transfer (LMCT) final states. The assignments of all observed inelastic scattering peaks to RIXS final states are summarized in Table 2. The relative intensities of the elastic and the inelastic scattering peaks  $1a_{M,L}$  and  $2a_{M,L}$  when excited at the metal  $a_M$  (705.6 eV) and the ligand  $a_L$  resonances (396.1 eV), which probe MOs with Fe 3d and N 2p character, respectively, change accordingly (elastic strong for  $a_M$  excitation, inelastic strongest for  $a_L$  excitation).

Our RASPT2 calculations of the Fe  $L_3$  RIXS spectra in Figure 6 confirm these assignments. They clearly show that the  $1a_M$  peak results due to decay from the  $5\sigma(e_g)$  MOs (Figure 6A1). The  $2a_M$  peak can correspond decay from the  $1\pi(t_{2g})$  MOs or from the  $4\sigma(e_g)$  MOs. Although the latter decay channels are not included in the RASPT2 RIXS calculation, the calculated SCF MOs indicate that both the  $1\pi(t_{2g})$  and  $4\sigma(e_g)$  MOs are lower in energy than  $5\sigma(e_g)$  MOs and there is a few percent of Fe 3d character mixed to  $1\pi(t_{2g})$  due to  $\pi$ -donation (Table S1). According to the calculations Fe 3d content of the  $4\sigma(e_g)$  MOs is below 1%, thus we assign the  $2a_M$  peak dominantly to decays from the  $1\pi(t_{2g})$  MOs. The inelastic  $1a_L$  and  $2a_L$  peaks for excitation at the N K-edge likely also correspond to decays from  $5\sigma(e_g)$  and  $1\pi(t_{2g})$  MOs, reflected in the almost identical energy transfer and spectral shapes as compared to the  $1a_M$  and  $2a_M$  peaks. However we note that decays from  $1\pi(t_{1g})$  and  $5\sigma(a_{1g})$  MOs are also possible at the  $a_L$  resonance.

In both ferri- and ferrocyanide the RIXS spectra for excitation at the  $b_M$  resonance at 710 eV (Figure 5A2 and 5B1) exhibit two intense and broad peaks denoted  $2b_M$  and  $3b_M$ . They are located at energy transfers of around 4 eV ( $2b_M$ ) and at around 8 eV ( $3b_M$ ). They respectively correspond to metal-centered (MC)  $[t_{2g},e_g]^5/[t_{2g},e_g]^6$  and LMCT  $[5\sigma(e_g)]^3[e_g]^1$  final states (Table 2). In ferricyanide the  $2b_M$  peak has a clear low-energy shoulder at an energy transfer of 3 eV. This feature, labeled as  $1b_M$ , can only be assigned

to quartet MC states (i.e. lowest-energy valence-excited states), which can be reached due to a significant mixing of states with different spin at the core-excited configuration due to 2p spin-orbit interaction (Figure 7). At the N K-edge, excitation to the  $b_L$  resonance at 398.5 eV leads to a dominating peak denoted  $3b_L$  and located at an energy transfer of 6.5 eV together with a clearly separated weaker  $2b_L$  peak at 4 eV. The energy of the latter matches exactly with the energy of the  $2b_M$  peak for excitation at the Fe  $L_3$ -edge. Therefore it is very likely that the  $2b_L$  peak corresponds to  $^2MC$  final states, suggesting that the  $b_L$  X-ray absorption resonance has considerable  $[N1s(t_{1u})]^5[t_{2g}]^5[e_g]^1$  character. The high intensity of the  $3b_L$  peak indicates, however, that excitations to  $2\pi$  still dominate at the  $b_L$  resonance, also due to the proximity to the  $c_L$  resonance.

We denote the most intense RIXS peak, for excitation at the  $c_M$  resonance at 712.5 eV, with  $2c_M$  and find it at 7 eV in ferricyanide and at 5 eV in ferrocyanide (Figure 5A3 and 5B2). These energies match well with the energies of the corresponding  $2c_L$  peaks of 7 eV in ferricyanide and 5 eV in ferrocyanide for excitation at the ligand  $c_L$  resonance of 399.6 eV. Based on our calculations (Figure 6) we assign these peaks to metal-to-ligand charge-transfer (MLCT) final states (Table 2). Given the complicated character of the  $c_M$  resonance, it is likely that scattering to higher-energy MC final states is possible (double and triple excitations to  $e_g$  orbitals gives rise to MC final states around 8 to 12 eV). Mixing with the low energy MC  $[t_{2g}]^{4/5}[e_g]^1$  states is apparent from the clearly distinguishable  $1c_M$  features at 3.25 eV energy transfers corresponding to  $^4MC/^3MC$  final states. The most intense RIXS peak for excitation at the  $c_L$  resonance at 399.6 eV is denoted  $3c_L$  and is located at 8 eV in ferricyanide and at 7.5 eV in ferrocyanide. Given that this peak is absent for excitation at the  $c_M$  resonance, the  $3c_L$  peak can be assigned to ligand-centered (LC)  $[5\sigma, 1\pi]^9[2\pi]^1$  final states, including decays from the nine  $1\pi(t_{1u}, t_{2u}, t_{1g})$  and four  $5\sigma(a_{1g}, t_{1u})$  non-bonding MOs that are not probed at the Fe  $L_3$ -edge. This is supported by SCF calculations which show that non-bonding  $1\pi(t_{1u}, t_{2u}, t_{1g})$  MOs have higher energy compared to bonding  $5\sigma(e_g)$  and  $1\pi(t_{2g})$  MOs (Table S1). The  $3c_L$  peak has a high energy tail denoted with  $4c_L$ , which overlaps in energy with the  $4c_M$  peak for excitation at the Fe  $L_3$ -edge. These features can thus be identified with LC final states corresponding to decays from bonding  $5\sigma(e_g)$  and  $1\pi(t_{2g})$  MOs (i.e. decay from same MOs as in case of  $1a_{M,L}/2a_{M,L}$  and  $3b_M$  RIXS features). The  $3c_L$  and  $4c_L$  peaks correspond to a collection of final states which can be reached via excitations involving N  $1s(a_{1g}, t_{1u}, e_g)$  core-holes while the MLCT final states of the  $2c_L$  peaks are only reached via core-excitations involving N  $1s(t_{1u})$  holes.

Comparison between ferri- and ferrocyanide shows that the LMCT  $[5\sigma(e_g)]^3[t_{2g}]^{5/6}[e_g]^1$  and the LC  $[1\pi(t_{1u}, t_{2u}, t_{1g})]^{17}[t_{2g}]^{5/6}[e_g]^0[2\pi]^1$  states (the  $3b_M$  and  $3c_L$  peaks, respectively) are relatively insensitive to the Fe charge state (i.e.  $t_{2g}$  occupation). In contrast, the MLCT  $[t_{2g}]^{4/5}[e_g]^0[2\pi(t_{2g})]^1$  and the LC  $[5\sigma(e_g)]^3[t_{2g}]^{5/6}[e_g]^0[2\pi(t_{2g})]^1$  final states (the  $2c_{M/L}$  and  $4c_{M/L}$  peaks, respectively) are higher in energy by about 1.5 – 2 eV in ferricyanide with respect to ferrocyanide. We find that this observation cannot be solely explained by the different ground state MO energies, but must be related to differences in how the different occupation of the  $t_{2g}$  manifold in the final states influence the energy of respective excitations. Using UV/vis absorption spectroscopy it was found that MLCT states have comparable energies in ferri- and ferrocyanide (Table S4). This could be explained by the fact the UV/vis absorption spectroscopy probes ungerade MLCT  $[t_{2g}]^{4/5}[e_g]^0[2\pi(t_{1u}, t_{2u})]^1$  states, whereas RIXS probes gerade MLCT  $[t_{2g}]^{4/5}[e_g]^0[2\pi(t_{2g})]^1$  states. Alternatively, it is also possible that UV/vis peaks assigned to MLCT states in ferricyanide actually correspond to LMCT states.

A detailed comparison of the experimental and calculated RIXS spectra is shown in Figure 6. The relative energies and intensities of the inelastic RIXS features are reproduced very well by the RASPT2 calculations. Particularly, in comparison to the CTM calculations the RASPT2 calculations describe better the features corresponding to decays from  $5\sigma(e_g)$  MOs ( $1a_M$ ,  $3b_M$ , and  $4c_M$  features). This indicates an improved description of  $\sigma$ -donation in the RASPT2 calculations. An apparently significant discrepancy between the experimental and calculated spectra is the overestimation of the elastic peak intensities. In ferricyanide the calculated elastic peak intensities are about two times higher than in the experiment, whereas in ferrocyanide the discrepancy is more than factor of ten. Although this can be due to inaccuracies in the calculations, there are several factors that influence the elastic peak intensity and that were not well controlled in our experiment or were not included in our simulations. These include vibrational effects, Thomson scattering, surface scattering and self-absorption effects.

In Figure 7A-B we present the spin decomposition of the XAS spectra according to the RASPT2 calculations. With the exception of the  $a_M$  resonance, the  $b_M$  and  $c_M$  resonances have strongly mixed spin character in both ferri- and ferrocyanide due to the 2p spin-orbit interaction. A decomposition of the RIXS maps according to the spin of the RIXS final state is shown in Figure 7C-F. The weak 3d spin-orbit interaction does not strongly mix the valence excited states, but final states with quartet/triplet multiplicity can be reached due to strong mixing of spin character in the intermediate core-excited states.

## Discussion

Disentangling donation and back-donation effects in ferri- and ferrocyanide is experimentally challenging, in principle requiring orbitally resolved methods that probe both occupied and unoccupied MOs. Effects of donation are manifested in X-ray absorption spectra indirectly as modifications of resonance energies and relative intensities (e.g. edge shifts and modifications of multiplet structures due to, e.g., the nephelauxetic effect or  $10Dq$ ), thus not having a unique spectroscopic signature (note that the well-known charge-transfer satellites in  $L_{2,3}$ -edge XAS of transition metal compounds only probe the change of donation between the ground and core-excited states<sup>55</sup>). In contrast, RIXS at the Fe  $L_3$  and the N K-edge is directly sensitive to the MOs relevant for quantifying the donation and back-donation effects. For ferri- and ferrocyanide, the RIXS peaks corresponding to LMCT and LC final states ( $1a_M/2a_M$ ,  $3b_M$  and  $4c_M$ ) reflect the Fe 3d character of nominally  $CN^-$   $5\sigma(e_g)$  and  $1\pi(t_{2g})$  MOs ( $\sigma$ - and  $\pi$ -donation, respectively). The peaks corresponding to MLCT final states for excitation at the N K-edge ( $2c_L$ ) in turn reflect the N 2p character of nominally Fe  $t_{2g}$  MOs ( $\pi$  back-donation).  $\pi$  back-donation can also be directly probed by analyzing XAS at the Fe  $L_3$ -edge and inspecting the resonance corresponding to excitations to  $2\pi(t_{2g})$  MOs ( $c_M$  resonance) or at the N K-edge if the  $t_{2g}$  manifold is partially filled, like in the case of ferricyanide ( $a_L$  resonance). Therefore a combined RIXS/XAS experiment at the Fe  $L_3$ -edge is directly sensitive to both donation and back-donation.

Quantification of these interactions requires high-level simulations due to overlapping spectral features and due to the presence of several multiplet, configuration interaction and core-hole relaxation effects. All of these effects are taken into account in our RASPT2 calculations. Given the very good agreement of our calculations with the measured XAS and RIXS data we can now proceed to interpreting experimental observables with the RASPT2 calculations to extract a consistent picture of chemical bonding in ferri- and ferrocyanide in solution.

Table 3 summarizes the covalent chemical bonding effects in terms of decompositions of the relevant valence MOs into Fe 3d, N 2p and C 2p contributions. The contributions are calculated based on respective squared atomic orbital coefficient (e.g. coefficients corresponding to five Fe 3d atomic orbitals) and dividing them by the sum of all the squared atomic orbital coefficients of the MO (i.e. normalization to 1). For ferri- and ferrocyanide we deduce from the relative amount of Fe d character strong  $\sigma$ -donation (29% vs. 20% in  $5\sigma(e_g)$ , respectively). We also find weak  $\pi$ -donation ( $\sim 1\%$  in  $1\pi(t_{2g})$  in both complexes) and considerable  $\pi$ -back-donation (7% vs 9% in  $2\pi(t_{2g})$ , respectively).

Our calculations thus reveal that  $\sigma$ -donation is stronger in the ferric complex while  $\pi$ -back-donation is stronger in ferrous complex.  $\pi$ -donation is weak and approximately equal in both.

Our analysis is consistent with the results from infrared spectroscopy where it has been established that  $\sigma$ -donation increases and  $\pi$ -back-donation decreases when the effective metal charge increases (or when the d electron count decreases).<sup>56</sup> Experimentally this is manifested in higher C-N stretch frequencies in ferricyanide with respect to ferrocyanide.

In Table 4 we compare our results for ferric and ferrous hexacyanide in terms of metal-ligand covalency with the previous X-ray spectroscopy studies. We note that although quantitative comparison of the covalency values between different methods is not accurate, the trends in covalencies within a method still provide valuable electronic structure information. The overall magnitude of  $\sigma$ -donation matches well with the DFT calculations published by Hocking et al.<sup>17</sup> However, in contrast to our results their calculations exhibit the same Fe 3d content in the  $5\sigma(e_g)$  MOs of ferric and ferrous hexacyanide. Also, we find considerably weaker  $\pi$ -donation compared to Hocking et al. Compared to the RASSCF results from Engel et al. our calculations give less  $\sigma$ -donation.<sup>16</sup> The DFT and Valence Bond Configuration Interaction (VBCI) results from Hocking et al.<sup>17</sup> and Lundberg et al.<sup>18</sup> show  $\pi$ -back-donation to be larger by approximately a factor of 2 compared to the RASPT2 results presented here. Additionally, no considerable difference in  $\pi$ -back-donation between ferri- and ferrocyanide was found. These discrepancies in characterizing the  $2\pi(t_{2g})$  composition could be attributed to the fact that the DFT and VBCI results refer to the overall Fe d character and not only to the Fe 3d character. There is a very good agreement between the values of overall Fe d contribution to the  $2\pi(t_{2g})$  MOs retrieved in this work (Table S3) and the values presented in Hocking et al. and in Lundberg et al. (note however that the results of Engel et al. are still considerably higher). Only for the  $2\pi(t_{2g})$  MO the Fe  $4d(t_{2g})$  and  $5d(t_{2g})$  contributions become considerable. We find that the Fe d character of the other MOs listed in Table 3 is mostly due to Fe 3d orbitals (Table S3).

Our RASPT2 calculations further reveal considerable core-hole induced effects to the Fe 3d content of the valence MOs.  $\sigma$ -donation to the  $5\sigma(e_g)$  MO is considerably increased upon Fe 2p core-hole screening, whereas  $\pi$ -back-donation is decreased (Table 3). Latter effects can be explained by considering the lowering of  $t_{2g}$  and  $e_g$  MO energies due to core-hole potential which results in decrease of  $5\sigma(e_g)$  and  $e_g$  energetic distance and increase of the energetic distance between  $t_{2g}$  and  $2\pi(t_{2g})$  MOs. Interestingly, the overall

Fe d content to the  $2\pi(t_{2g})$  MOs in ferricyanide increases as a result of Fe 2p core-hole screening while in ferrocyanide the Fe d content decreases (Table S3).

## **Summary**

Utilizing Fe  $L_{2,3}$  and N K-edge RIXS we have mapped out the valence excited states of ferric and ferrous hexacyanide. The task of identification and characterization of the valence excited state spectrum in transition metal complexes is often a challenge for more conventional UV/vis absorption spectroscopy due to high density of overlapping states, large differences in absorption cross sections and the extension of state energies to the vacuum ultraviolet region. Here, combining the metal and the ligand views allowed to identify the metal-centered, the ligand-to-metal, the metal-to-ligand and the ligand-centered excited states and to quantify their relative energetics.

The high sensitivity of RIXS at the Fe  $L_{2,3}$ -edge to chemical bonding has been demonstrated before.<sup>16,57,58</sup> However, disentangling donation and back-donation effects from multiplet, configuration interaction and core-hole relaxation effects is a challenging task which we have resolved here with quantum chemical RASPT2 calculations. This allowed us to quantify the donation and back-donation interactions in ferric and ferrous hexacyanide aqueous solutions with unprecedented detail. Our results agree with previous infrared spectroscopy studies that have shown that the increase of the effective Fe charge increases donation and decreases back-donation.

The presented investigation demonstrates the potential of soft X-ray RIXS for detailed studies of local chemical bonding of functional transition metal compounds, as well as for time-resolved studies of the excited states of photoactive materials.

## **Acknowledgements**

K.K. acknowledges Thomas Kroll and Marco Reinhard for fruitful discussions and Robert Green for generously providing a program to carry out the CTM calculations. K.K. and P.S.M. acknowledge Frank de Groot for providing the input files for the CTM calculations. M.L. would like to thank Erik Källman for help in analyzing the RAS calculations. We gratefully acknowledge the continuous support by the BESSYII staff and we thank HZB for the allocation of synchrotron radiation beamtime. Portions of the presented research were funded by the Helmholtz Virtual Institute “Dynamic Pathways in Multidimensional Landscapes”. This work was further supported by the Swedish Research Council (M.L. and M.O.), the Carl Tryggers Foundation (R.P. and M.O.) and Knut and Alice Wallenberg Foundation, Grant No. KAW-2013.0020 (M.L.). W.Z. and K.J.G. acknowledge support through the AMOS program within the Chemical Sciences, Geosciences, and Biosciences

Division of the Office of Basic Energy Sciences, Office of Science, U.S. Department of Energy. The simulations were in part performed on resources provided by the Swedish National Infrastructure for Computing (SNIC) at the Swedish National Supercomputer Center (NSC), the High Performance Computer Center North (HPC2N) and Chalmers Centre for Computational Science and Engineering (C3SE).

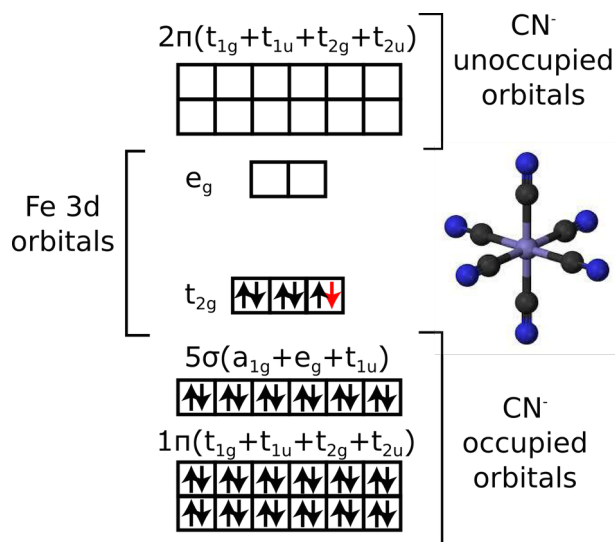


**Figure 1.** Qualitative valence molecular-orbital (MO) diagram of an octahedral iron hexacyanide complex with Fe-centered nominal 3d and ligand-centered CN<sup>-</sup> MOs. The ferrous complex (Fe<sup>2+</sup>, 3d<sup>6</sup>) has completely occupied  $t_{2g}$  MOs, whereas the ferric complex (Fe<sup>3+</sup>, 3d<sup>5</sup>) has a hole at the  $t_{2g}$  MOs (note the red electron for the ferrous complex).

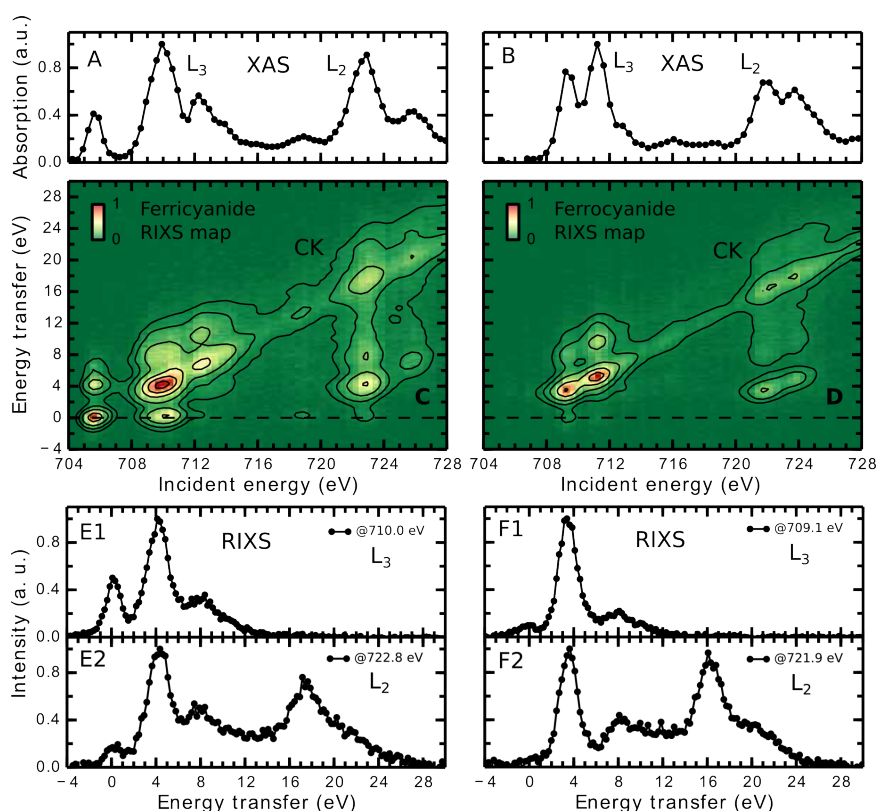


**Figure 2.** Experimental Fe  $L_{2,3}$ -edge RIXS of Ferri- and ferrocyanide. Partial Fluorescence yield (PFY)-XAS (A and B), RIXS maps (C and D) and RIXS spectra (E and F) of ferri- and ferrocyanide. The features denoted CK result from fluorescence decays preceded by Coster-Kronig decays. Normalized intensities in the RIXS planes are encoded in color where green corresponds to zero and red to one. The RIXS spectra correspond to vertical cuts through the RIXS planes and are shown for the given incident photon energy ranges corresponding to the PFY-XAS maxima of the  $L_3$  and  $L_2$  edges.

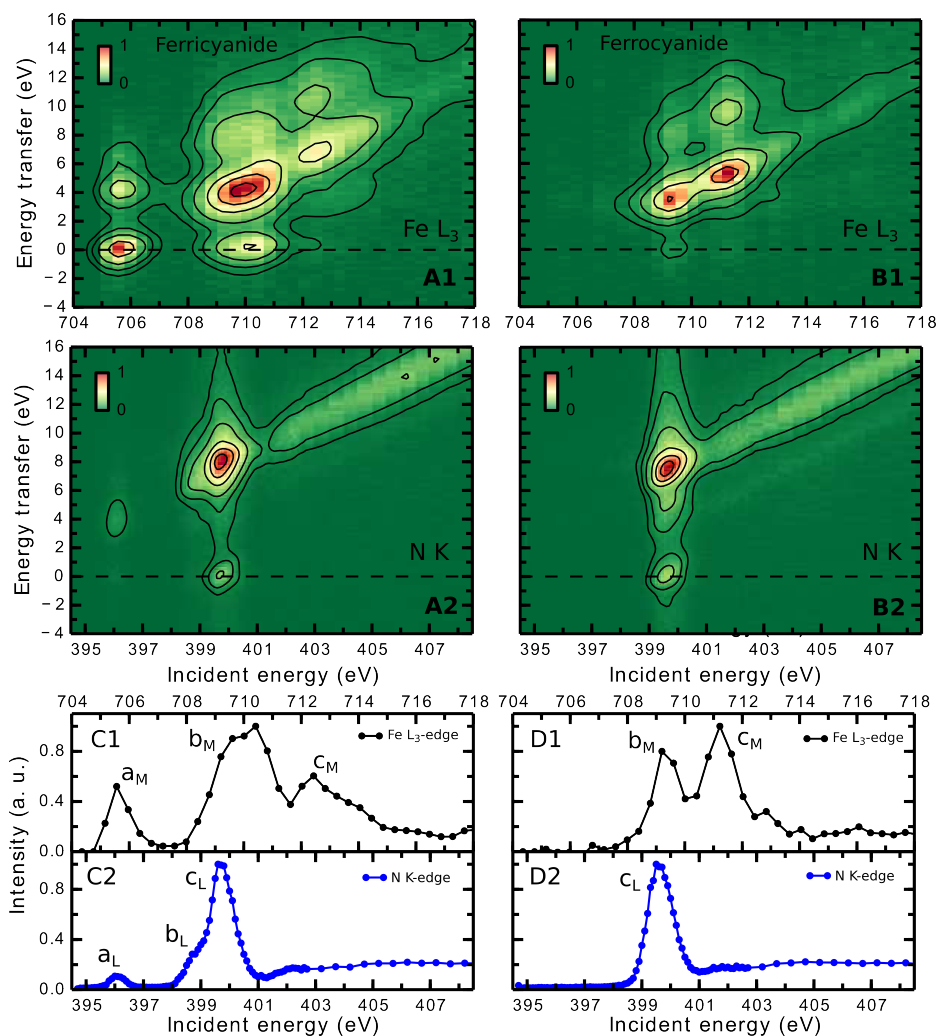


**Figure 3.** Experimental Fe L<sub>3</sub>-edge and N K-edge RIXS and XAS spectra. (A1) RIXS map of ferricyanide at the Fe L<sub>3</sub>-edge and (A2) at the N K-edge. (B1) RIXS map of ferrocyanide at the Fe L<sub>3</sub>-edge and (B2) at the N K-edge. PFY-XAS of (C) ferricyanide and (D) ferrocyanide. Note that incident photon energies are consistent in all panels. The displayed incident photon energy ranges at the Fe L<sub>3</sub>-edge and at the N K-edge are chosen to line up at the lowest energy XAS resonance of ferricyanide.

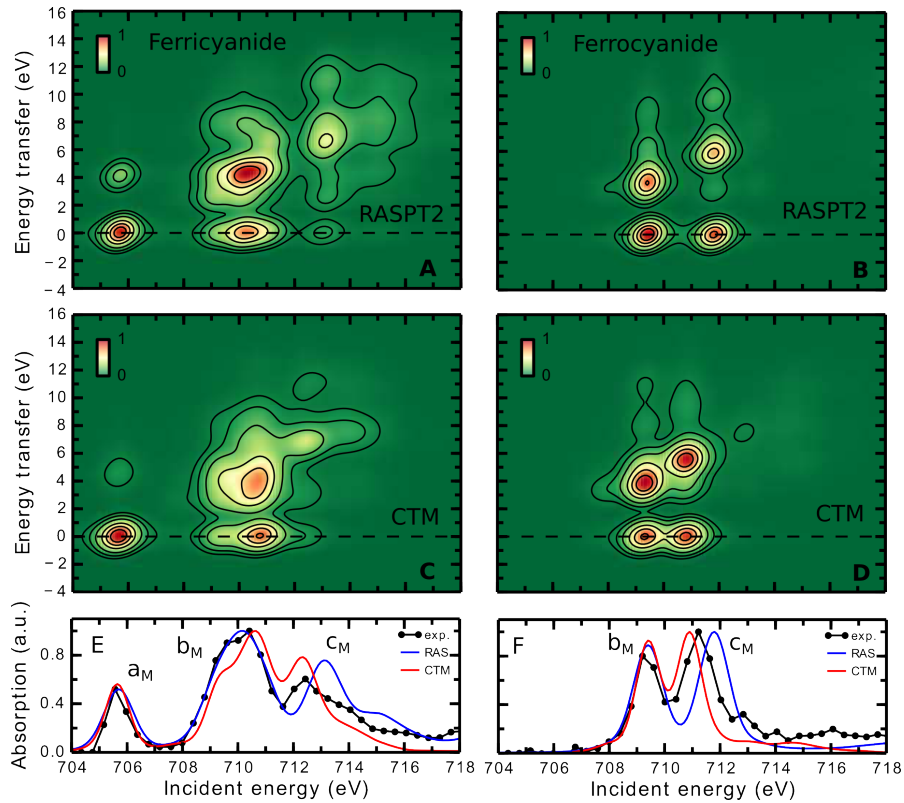


**Figure 4.** Comparison of experimental and calculated RIXS maps and XAS spectra at the Fe  $L_3$ -edge. Calculated RIXS maps of (A) ferricyanide and (B) ferrocyanide using the *ab initio* RASPT2 method. Calculated RIXS maps of (C) ferricyanide and (D) ferrocyanide using the semi-empirical CTM method and comparison PFY-XAS experimental and calculated spectra for ferricyanide (E) and ferrocyanide (F).

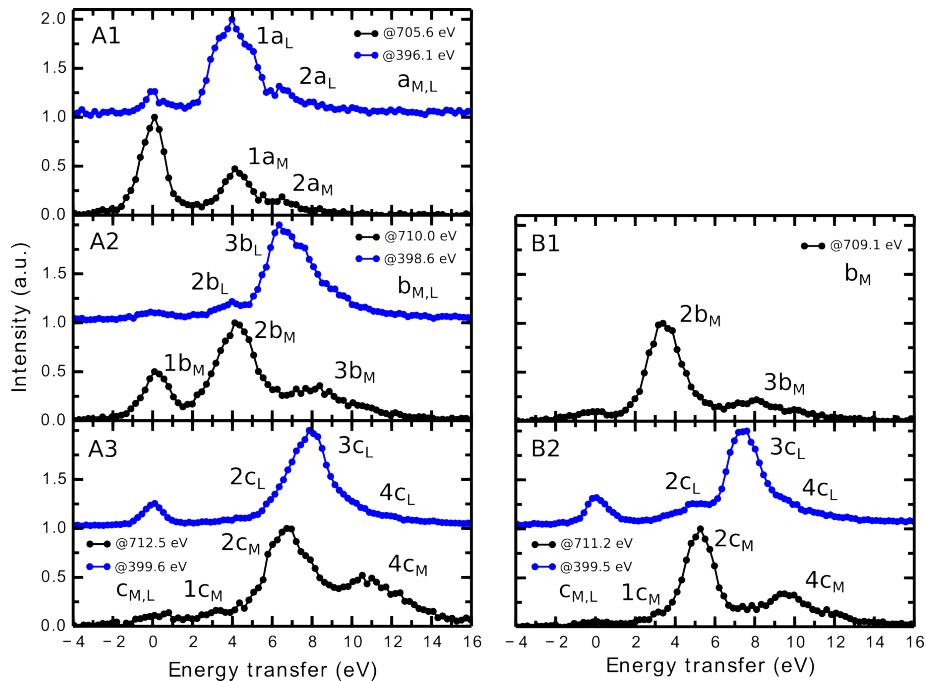


**Figure 5.** Experimental RIXS spectra at the selected X-ray absorption resonances. RIXS spectra of (A) ferricyanide and (B) ferrocyanide at the selected X-ray absorption resonances. RIXS spectra taken at the Fe  $L_3$  and at the N K-edges are directly compared.

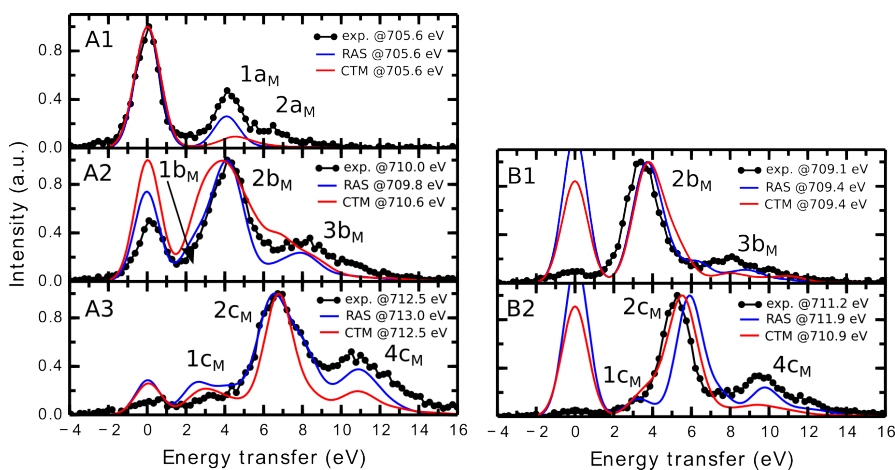


**Figure 6.** Comparison of experimental and calculated RIXS spectra at the selected X-ray absorption resonances at the Fe  $L_3$ -edge of (A) ferricyanide and (B) ferrocyanide.

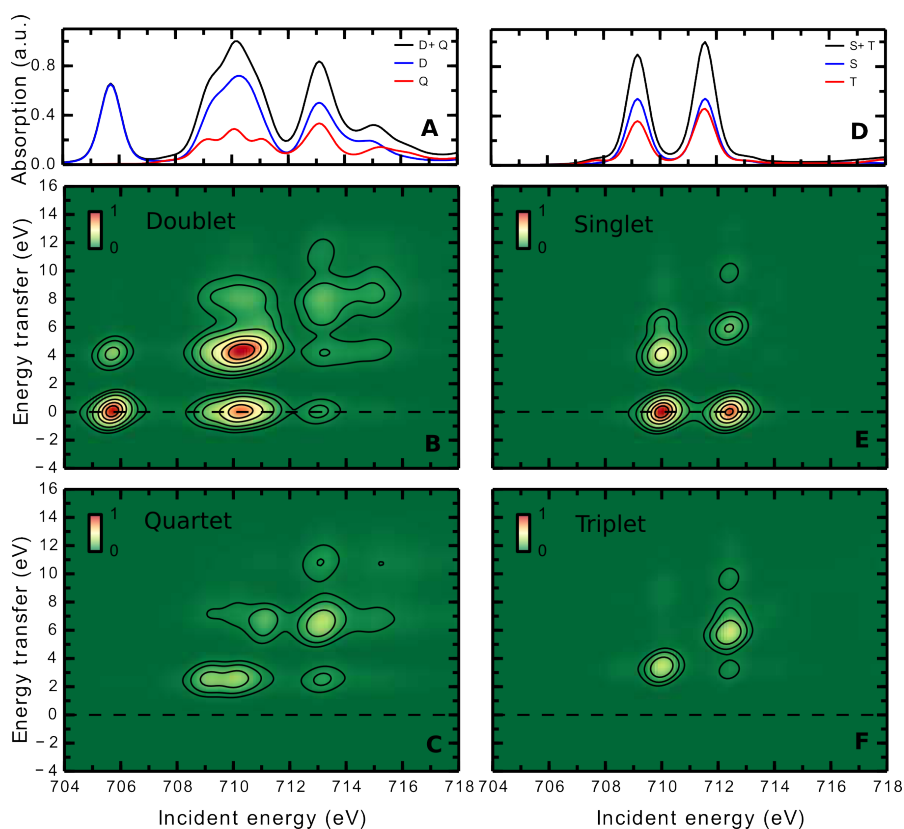


**Figure 7.** Spin decomposition of XAS and RIXS RASPT2 calculations. Ferricyanide (A) decomposed XAS spectra (D – doublet, Q – quartet), (B) doublet RIXS final states and (C) quartet RIXS final states. Ferrocyanide (A) decomposed XAS spectra (S – singlet, T – triplet), (B) singlet RIXS final states and (C) triplet RIXS final states.

**Table 1.** Energies and assignments of measured X-ray absorption resonances based on Refs. <sup>14,17,34</sup> and calculations in this work for ferric and ferrous hexacyanide and for resonances  $a_M$ - $c_M$  at the Fe  $L_3$  and  $a_L$ - $c_L$  the N K-edge (see Figure 1 for labels of molecular orbitals).

Resonance	$[\text{Fe}(\text{CN})_6]^{3-}$		$[\text{Fe}(\text{CN})_6]^{4-}$	
	Energy (eV)	Assignment	Energy (eV)	Assignment
Fe $L_3$ -edge				
$a_M$	705.6	$[\text{Fe}2p(t_{1u})]^5[t_{2g}]^6[e_g]^0$	-	-
$b_M$	710.0	$[\text{Fe}2p(t_{1u})]^5[t_{2g}]^5[e_g]^1$	709.1	$[\text{Fe}2p(t_{1u})]^5 \dots [t_{2g}]^6[e_g]^1$
$c_M$	712.5	$[\text{Fe}2p(t_{1u})]^5[t_{2g}]^5[e_g]^0[2\pi(t_{2g})]^1$ $[\text{Fe}2p(t_{1u})]^5[t_{2g}]^4[e_g]^2$ $[\text{Fe}2p(t_{1u})]^5[5\sigma(e_g)]^3[t_{2g}]^6[e_g]^1$	711.2	$[\text{Fe}2p(t_{1u})]^5[t_{2g}]^6[e_g]^0[2\pi(t_{2g})]^1$ $[\text{Fe}2p(t_{1u})]^5[t_{2g}]^4[e_g]^2$
N K-edge				
$a_L$	396.1	$[\text{N}1s(t_{1u})]^5[t_{2g}]^6[e_g]^0$	-	-
$b_L$	398.5	$[\text{N}1s(t_{1u})]^5[t_{2g}]^5[e_g]^1$	-	-
$c_L$	399.6	$[\text{N}1s(a_{1g}, t_{1u}, e_g)]^{11}[t_{2g}]^5[e_g]^0[2\pi]^1$	399.5	$[\text{N}1s(a_{1g}, t_{1u}, e_g)]^{11}[t_{2g}]^6[e_g]^0[2\pi]^1$

**Table 2.** Energies and assignments of RIXS peaks based on the comparison of the experiments and calculations in this work for ferric and ferrous hexacyanide and for excitations at the Fe  $L_3$  and the N K-edge (see Figure 1 for labels of molecular orbitals).

Peak	$[\text{Fe}(\text{CN})_6]^{3-}$		$[\text{Fe}(\text{CN})_6]^{4-}$	
	Energy (eV)	Assignment	Energy (eV)	Assignment
Fe $L_3$ -edge				
$1a_M$	4	${}^2\text{LMCT}$ $[5\sigma(e_g)]^3[t_{2g}]^6$	-	-
$2a_M$	~7	${}^2\text{LMCT}$ $[1\pi(t_{2g})]^5[t_{2g}]^6$	-	-
$1b_M$	3	${}^4\text{MC}$ $[t_{2g}]^4[e_g]^1$	-	-
$2b_M$	4	${}^2\text{MC}$ $[t_{2g}]^4[e_g]^1$	3.5	${}^1\text{MC}$ $[t_{2g}]^5[e_g]^1$
$3b_M$	8.5	${}^{2,4}\text{LMCT}$ $[5\sigma(e_g)]^3[t_{2g}]^5[e_g]^1$ $[1\pi(t_{2g})]^5[t_{2g}]^5[e_g]^1$	8	${}^{1,3}\text{LMCT}$ $[5\sigma(e_g)]^3[t_{2g}]^6[e_g]^1$ $[1\pi(t_{2g})]^5[t_{2g}]^6[e_g]^1$
$1c_M$	3.25	${}^4\text{MC}$ $[t_{2g}]^4[e_g]^1$	3.25	${}^3\text{MC}$ $[t_{2g}]^5[e_g]^1$
$2c_M$	7	${}^{2,4}\text{MLCT}$ $[t_{2g}]^4[e_g]^0[2\pi(t_{2g})]^1$	5	${}^{1,3}\text{MLCT}$ $[t_{2g}]^5[e_g]^0[2\pi(t_{2g})]^1$
$4c_M$	11	${}^{2,4}\text{LC}$ $[5\sigma(e_g)]^3[t_{2g}]^5[e_g]^0[2\pi(t_{2g})]^1$ $[1\pi(t_{2g})]^5[t_{2g}]^5[e_g]^0[2\pi(t_{2g})]^1$	9.5	${}^{1,3}\text{LC}$ $[5\sigma(e_g)]^3[t_{2g}]^6[e_g]^0[2\pi(t_{2g})]^1$ $[1\pi(t_{2g})]^5[t_{2g}]^6[e_g]^0[2\pi(t_{2g})]^1$
N K-edge				
$1a_L$	4	${}^2\text{LMCT}$ $[5\sigma(e_g)]^3[t_{2g}]^6$ $[1\pi(t_{1g})]^5[t_{2g}]^6$	-	-
$2a_L$	~7	${}^2\text{LMCT}$ $[1\pi(t_{2g})]^5[t_{2g}]^6$ $[5\sigma(a_{1g})]^1[t_{2g}]^6$	-	-
$2b_L$	4	${}^2\text{MC}$ $[t_{2g}]^4[e_g]^1$	-	-
$3b_L$	6.5	${}^2\text{LMCT}$ and/or ${}^2\text{MLCT}$ $[5\sigma(e_g)]^3[t_{2g}]^5[e_g]^1/$ $[t_{2g}]^4[e_g]^0[2\pi]^1$	-	-

2c <sub>L</sub>	7	<sup>2</sup> MLCT [t <sub>2g</sub> ] <sup>4</sup> [e <sub>g</sub> ] <sup>0</sup> [2π(t <sub>2g</sub> )] <sup>1</sup>	5	<sup>1</sup> MLCT [t <sub>2g</sub> ] <sup>5</sup> [e <sub>g</sub> ] <sup>0</sup> [2π(t <sub>2g</sub> )] <sup>1</sup>
3c <sub>L</sub>	8	<sup>2</sup> LC [1π(t <sub>1u</sub> ,t <sub>2u</sub> ,t <sub>1g</sub> )] <sup>17</sup> [t <sub>2g</sub> ] <sup>5</sup> [e <sub>g</sub> ] <sup>0</sup> [2π] <sup>1</sup>	7.5	<sup>1</sup> LC [1π(t <sub>1u</sub> ,t <sub>2u</sub> ,t <sub>1g</sub> )] <sup>17</sup> [t <sub>2g</sub> ] <sup>6</sup> [e <sub>g</sub> ] <sup>0</sup> [2π] <sup>1</sup>
4c <sub>L</sub>	~11	<sup>2</sup> LC [5σ] <sup>11</sup> [t <sub>2g</sub> ] <sup>5</sup> [e <sub>g</sub> ] <sup>0</sup> [2π] <sup>1</sup> [1π(t <sub>2g</sub> )] <sup>5</sup> [t <sub>2g</sub> ] <sup>5</sup> [e <sub>g</sub> ] <sup>0</sup> [2π] <sup>1</sup>	~10	<sup>1</sup> LC [5σ] <sup>11</sup> [t <sub>2g</sub> ] <sup>6</sup> [e <sub>g</sub> ] <sup>0</sup> [2π] <sup>1</sup> [1π(t <sub>2g</sub> )] <sup>5</sup> [t <sub>2g</sub> ] <sup>6</sup> [e <sub>g</sub> ] <sup>0</sup> [2π] <sup>1</sup>

**Table 3.** Decomposition of valence molecular orbitals into the contributions of atomic orbitals with Fe 3d, N 2p and C 2p character for ferric and ferrous hexacyanide. Values are deduced from the RASPT2 calculations based on the normalized squared atomic orbital coefficients of valence molecular orbitals. Values are averaged over individual D<sub>2h</sub> symmetry-adapted molecular orbitals and over states with different symmetries. Numbers in front (in the parenthesis correspond to contributions in the electronic ground states (in the presence of a Fe 2p core-hole).

Molecular orbital	[Fe(CN) <sub>6</sub> ] <sup>3-</sup>			[Fe(CN) <sub>6</sub> ] <sup>4-</sup>		
	Fe 3d	N 2p	C 2p	Fe 3d	N 2p	C 2p
5σ(a <sub>1g</sub> ,t <sub>1u</sub> )	0.0(0.0)	45.5(45.4)	25.6(26.4)	0.0(0.0)	47.5(47.5)	25.3(26.2)
1π(t <sub>2g</sub> )	1.4(1.4)	59.8(60.7)	37.9(37.1)	1.1(1.0)	63.8(64.6)	33.9(33.2)
5σ(e <sub>g</sub> )	28.9(48.9)	10.7(8.4)	24.0(28.3)	20.1(37.5)	10.1(9.3)	20.8(27.2)
1π(t <sub>1u</sub> ,t <sub>2u</sub> ,t <sub>1g</sub> )	0.0(0.0)	43.6(43.7)	22.4(22.2)	0.0(0.0)	46.1(46.2)	19.6(19.5)
t <sub>2g</sub>	93.9(95.2)	5.6(3.5)	0.1(0.2)	90.9(94.4)	7.8(4.5)	0.7(0.0)
e <sub>g</sub>	40.4(24.8)	3.2(3.5)	12.1(7.2)	37.4(23.7)	3.3(3.3)	6.7(4.2)
2π(t <sub>2g</sub> )	6.8(4.3)	45.1(42.3)	33.7(30.2)	9.4(6.0)	41.5(42.8)	37.0(39.1)
2π(t <sub>1u</sub> ,t <sub>2u</sub> ,t <sub>1g</sub> )	0.0(0.0)	26.8(27.0)	47.1(47.3)	0.0(0.0)	27.2(27.2)	49.4(49.4)

**Table 4.** Comparison of metal-ligand covalency in ferric and ferrous cyanide in terms of % of Fe 3d character in the valence molecular orbitals from this work and compared to previous studies.

Molecular orbital	[Fe(CN) <sub>6</sub> ] <sup>3-</sup>			[Fe(CN) <sub>6</sub> ] <sup>4-</sup>			
	This work	DFT <sup>a</sup>	VBCI <sup>b</sup>	This work	DFT <sup>a</sup>	VBCI <sup>b</sup>	RASSCF <sup>c</sup>
1π(t <sub>2g</sub> )	1.4	10	-	1.1	8	-	-
5σ(e <sub>g</sub> )	28.9	28	-	20.1	28	-	33.1
t <sub>2g</sub>	93.9	77	62	90.9	77	-	98.5
e <sub>g</sub>	40.4	54	52	37.4	57	58	34.9
2π(t <sub>2g</sub> )	6.8	14	13	9.4	16	14	55.4

<sup>a</sup> BP86 DFT calculations from Figure 11 in Ref. 17.

<sup>b</sup>Valence Bond Configuration Interaction (VBCI) results from Table S3 in the Supporting Information of Ref. 18.

<sup>c</sup> Restricted Active Space Self Consistent Field (RASSCF) calculations from Table 1 in Ref. 16.

## References

- (1) Silberberg, M. In *Principles of General Chemistry*; 2009; pp 2837–2861.
- (2) Gray, H. B. *Proc. Natl. Acad. Sci. U. S. A.* **2003**, *100* (7), 3563.
- (3) Lippard, S. J. *Nat. Chem. Biol.* **2006**, *2* (10), 504.
- (4) Solomon, E. I.; Szilagyi, R. K.; DeBeer George, S.; Basumallick, L. *Chem. Rev.* **2004**, *104* (2), 419.
- (5) Solomon, E. I.; Heppner, D. E.; Johnston, E. M.; Ginsbach, J. W.; Cirera, J.; Qayyum, M.; Kieber-Emmons, M. T.; Kjaergaard, C. H.; Hadt, R. G.; Tian, L. *Chem. Rev.* **2014**, *114* (7), 3659.
- (6) Zhang, M.; de Respinis, M.; Frei, H. *Nat. Chem.* **2014**, *6* (4), 362.
- (7) Stöhr, J. *NEXAFS Spectroscopy*; Springer: Berlin, 1992.
- (8) de Groot, F. M. F.; Kotani, A. *Core Level Spectroscopy of Solids*; CRC Press: Boca Raton, 2008.
- (9) Solomon, E. I.; Hedman, B.; Hodgson, K. O.; Dey, A.; Szilagyi, R. K. *Coord. Chem. Rev.* **2005**, *249* (1-2), 97.
- (10) Vannerberg, N.-G. *Acta Chem. Scand.* **1972**, *26*, 2863.
- (11) Taylor, J. C.; Mueller, M. H.; Hitterman, R. L. *Acta Crystallogr. Sect. A* **1970**, *26* (5), 559.
- (12) Obashi, M. *Jpn. J. Appl. Phys.* **1978**, *17* (3), 563.
- (13) Bianconi, A.; Dell’Ariccia, M.; Durham, P. J.; Pendry, J. B. *Phys. Rev. B* **1982**, *26* (12), 6502.
- (14) Vinogradov, A. S.; Preobrajenski, A. B.; Knop-Gericke, A.; Molodtsov, S. L.; Krasnikov, S. A.; Nekipelov, S. V.; Szargan, R.; Hävecker, M.; Schlögl, R. *J. Electron Spectros. Relat. Phenomena* **2001**, *114-116*, 813.
- (15) Freiwald, M.; Cramm, S.; Eberhardt, W.; Eisebitt, S. *J. Electron Spectros. Relat. Phenomena* **2004**, *137-140*, 413.
- (16) Engel, N.; Bokarev, S. I.; Suljoti, E.; Garcia-Diez, R.; Lange, K. M.; Atak, K.; Golnak, R.; Kothe, A.; Dantz, M.; Kühn, O.; Aziz, E. F. *J. Phys. Chem. B* **2014**, *118* (6), 1555.
- (17) Hocking, R. K.; Wasinger, E. C.; de Groot, F. M. F.; Hodgson, K. O.; Hedman, B.; Solomon, E. I. *J. Am. Chem. Soc.* **2006**, *128* (32), 10442.
- (18) Lundberg, M.; Kroll, T.; Debeer, S.; Bergmann, U.; Wilson, S. a.; Glatzel, P.; Nordlund, D.; Hedman, B.; Hodgson, K. O.; Solomon, E. I. *J. Am. Chem. Soc.* **2013**, *135* (45), 17121.
- (19) Penfold, T. J.; Reinhard, M.; Rittmann-Frank, M. H.; Tavernelli, I.; Rothlisberger, U.; Milne, C. J.; Glatzel, P.; Chergui, M. *J. Phys. Chem. A* **2014**, *118* (40), 9411.
- (20) Lee, N.; Petrenko, T.; Bergmann, U.; Neese, F.; DeBeer, S. *J. Am. Chem. Soc.* **2010**, *132* (28), 9715.
- (21) Pollock, C. J.; Delgado-Jaime, M. U.; Atanasov, M.; Neese, F.; DeBeer, S. *J. Am. Chem. Soc.* **2014**, *136* (26), 9453.
- (22) Reinhard, M.; Penfold, T. J.; Lima, F. a.; Rittmann, J.; Rittmann-Frank, M. H.; Abela, R.; Tavernelli, I.; Rothlisberger, U.; Milne, C. J.; Chergui, M. *Struct. Dyn.* **2014**, *1*, 024901.

- (23) March, A. M.; Assefa, T. A.; Bressler, C.; Doumy, G.; Galler, A.; Gawelda, W.; Kanter, E. P.; Németh, Z.; Pápai, M.; Southworth, S. H.; Young, L.; Vankó, G. *J. Phys. Chem. C* **2015**, *119* (26), 14571.
- (24) Risch, M.; Stoerzinger, K. A.; Regier, T. Z.; Peak, D.; Sayed, S. Y.; Shao-Horn, Y. *J. Phys. Chem. C* **2015**, *119* (33), 18903.
- (25) Westre, T. E.; Kennepohl, P.; DeWitt, J. G.; Hedman, B.; Hodgson, K. O.; Solomon, E. *J. Am. Chem. Soc.* **1997**, *119* (27), 6297.
- (26) Glatzel, P.; Bergmann, U. *Coordination Chemistry Reviews*. 2005, pp 65–95.
- (27) Guo, J. H.; Luo, Y.; Augustsson, A.; Rubensson, J. E.; Sàthe, C.; Ågren, H.; Siegbahn, H.; Nordgren, J. *Phys. Rev. Lett.* **2002**, *89*, 137402.
- (28) Guo, J.; Tong, T.; Svec, L.; Go, J.; Dong, C.; Chiou, J.-W. *J. Vac. Sci. Technol. A* **2007**, *25*, 1231.
- (29) Lange, K. M.; Könnecke, R.; Ghadimi, S.; Golnak, R.; Soldatov, M. A.; Hodeck, K. F.; Soldatov, A.; Aziz, E. F. *Chem. Phys.* **2010**, *377*, 1.
- (30) Lange, K. M.; Kothe, A.; Aziz, E. F. *Phys. Chem. Chem. Phys.* **2012**, *14* (16), 5331.
- (31) Kunnus, K.; Rajkovic, I.; Schreck, S.; Quevedo, W.; Eckert, S.; Beye, M.; Suljoti, E.; Weniger, C.; Kalus, C.; Grübel, S.; Scholz, M.; Nordlund, D.; Zhang, W.; Hartsock, R. W.; Gaffney, K. J.; Schlotter, W. F.; Turner, J. J.; Kennedy, B.; Hennies, F.; Techert, S.; Wernet, P.; Föhlisch, A. *Rev. Sci. Instrum.* **2012**, *83*, 123109.
- (32) Josefsson, I.; Kunnus, K.; Schreck, S.; Föhlisch, A.; De Groot, F.; Wernet, P.; Odelius, M. *J. Phys. Chem. Lett.* **2012**, *3* (23), 3565.
- (33) Kunnus, K.; Josefsson, I.; Schreck, S.; Quevedo, W.; Miedema, P. S.; Techert, S.; De Groot, F. M. F.; Odelius, M.; Wernet, P.; Föhlisch, A. *J. Phys. Chem. B* **2013**, *117* (51), 16512.
- (34) Pinjari, R. V.; Delcey, M. G.; Guo, M.; Odelius, M.; Lundberg, M. *J. Chem. Phys.* **2014**, *141* (12), 124116.
- (35) Guo, M.; Sørensen, L. K.; Delcey, M. G.; Pinjari, R. V.; Lundberg, M. *Phys. Chem. Chem. Phys.* **2016**, *18* (4), 3250.
- (36) van Schooneveld, M. M.; DeBeer, S. *J. Electron Spectros. Relat. Phenomena* **2015**, *198*, 31.
- (37) Aquilante, F.; Autschbach, J.; Carlson, R. K.; Chibotaru, L. F.; Delcey, M. G.; De Vico, L.; Fdez Galván, I.; Ferré, N.; Frutos, L. M.; Gagliardi, L.; Garavelli, M.; Giussani, A.; Hoyer, C. E.; Li Manni, G.; Lischka, H.; Ma, D.; Malmqvist, P. Å.; Müller, T.; Nenov, A.; Olivucci, M.; Pedersen, T. B.; Peng, D.; Plasser, F.; Pritchard, B.; Reiher, M.; Rivalta, I.; Schapiro, I.; Segarra-Martí, J.; Stenrup, M.; Truhlar, D. G.; Ungur, L.; Valentini, A.; Vancoillie, S.; Veryazov, V.; Vysotskiy, V. P.; Weingart, O.; Zapata, F.; Lindh, R. *J. Comput. Chem.* **2016**, *37* (5), 506.
- (38) Pinjari, R. V.; Delcey, M. G.; Guo, M.; Odelius, M.; Lundberg, M. *J. Chem. Phys.* **2015**, *142* (6), 069901.
- (39) Pinjari, R. V.; Delcey, M. G.; Guo, M.; Odelius, M.; Lundberg, M. *J. Comput. Chem.* **2016**, *37*, 477.
- (40) Roos, B. O.; Lindh, R.; Malmqvist, P. A.; Veryazov, V.; Widmark, P. O. *J. Phys. Chem. A* **2004**, *108* (15), 2851.
- (41) Finley, J.; Malmqvist, P. A.; Roos, B. O.; Serrano-Andres, L. *Chem. Phys. Lett.* **1998**,

- 288 (2-4), 299.
- (42) Malmqvist, P. Å.; Rendell, A.; Roos, B. O. *J. Phys. Chem.* **1990**, *94* (14), 5477.
- (43) Malmqvist, P. A.; Pierloot, K.; Shahi, A. R. M.; Cramer, C. J.; Gagliardi, L. *J. Chem. Phys.* **2008**, *128* (20), 204109.
- (44) Malmqvist, P. Å.; Roos, B. O.; Schimmelpfennig, B. *Chem. Phys. Lett.* **2002**, *357* (3-4), 230.
- (45) Thole, B. T.; van der Laan, G.; Fuggle, J. C.; Sawatzky, G. A.; Karnatak, R. C.; Esteve, J.-M. *Phys. Rev. B* **1985**, *32* (8), 5107.
- (46) de Groot, F. M. F.; Fuggle, J. C.; Thole, B. T.; Sawatzky, G. A. *Phys. Rev. B* **1990**, *42* (9), 5459.
- (47) Kurian, R.; Kunnus, K.; Wernet, P.; Butorin, S. M.; Glatzel, P.; de Groot, F. M. F. *J. Phys. Condens. Matter* **2012**, *24* (45), 452201.
- (48) Wernet, P.; Kunnus, K.; Schreck, S.; Quevedo, W.; Kurian, R.; Techert, S.; De Groot, F. M. F.; Odelius, M.; Föhlisch, A. *J. Phys. Chem. Lett.* **2012**, *3* (23), 3448.
- (49) Gotz, M. D.; Soldatov, M. A.; Lange, K. M.; Engel, N.; Golnak, R.; Könnecke, R.; Atak, K.; Eberhardt, W.; Aziz, E. F. *J. Phys. Chem. Lett.* **2012**, *3* (12), 1619.
- (50) Naiman, C. S. *J. Chem. Phys.* **1961**, *35* (1), 323.
- (51) Gray, H. B.; Beach, N. A. *J. Am. Chem. Soc.* **1963**, *85* (19), 2922.
- (52) Cramer, S. P.; de Groot, F. M. F.; Ma, Y.; Chen, C. T.; Sette, F.; Kipke, C. A.; Eichhorn, D. M.; Chan, M. K.; Armstrong, W. H.; Libby, E.; Christou, G.; Brooker, S.; Mckee, V.; Mullins, O. C.; Fuggle, J. C. *J. Am. Chem. Soc.* **1991**, *113* (21), 7937.
- (53) Butorin, S. M. *J. Electron Spectros. Relat. Phenomena* **2000**, *110-111*, 213.
- (54) van Schooneveld, M. M.; Gosselink, R. W.; Eggenhuisen, T. M.; Al Samarai, M.; Monney, C.; Zhou, K. J.; Schmitt, T.; de Groot, F. M. F. *Angew. Chem. Int. Ed. Engl.* **2013**, *52* (4), 1170.
- (55) de Groot, F. M. F. *J. Electron Spectrosc. Relat. Phenom.* **1994**, *67* (4), 529.
- (56) Jones, L. H. *Inorg. Chem.* **1963**, *2* (4), 777.
- (57) Suljoti, E.; Garcia-Diez, R.; Bokarev, S. I.; Lange, K. M.; Schoch, R.; Dierker, B.; Dantz, M.; Yamamoto, K.; Engel, N.; Atak, K.; Kühn, O.; Bauer, M.; Rubensson, J. E.; Aziz, E. F. *Angew. Chemie - Int. Ed.* **2013**, *52* (37), 9841.
- (58) Wernet, P.; Kunnus, K.; Josefsson, I.; Rajkovic, I.; Quevedo, W.; Beye, M.; Schreck, S.; Grübel, S.; Scholz, M.; Nordlund, D.; Zhang, W.; Hartsock, R. W.; Schlotter, W. F.; Turner, J. J.; Kennedy, B.; Hennies, F.; de Groot, F. M. F.; Gaffney, K. J.; Techert, S.; Odelius, M.; Föhlisch, A. *Nature* **2015**, *520* (7545), 78.